Biosensors and Bioelectronics 213 (2022) 114445

Contents lists available at ScienceDirect

Biosensors and Bioelectronics

journal homepage: www.elsevier.com/locate/bios

Bimodal liquid biopsy for cancer immunotherapy based on peptide engineering and nanoscale analysis

Jiyoon Bu [a,b,1], Woo-jin Jeong [a,b,1], Roya Jafari [c], Luke J. Kubiatowicz [a], Ashita Nair [a], Michael J. Poellmann [a], Rachel S. Hong [a], Elizabeth W. Liu [a], Randall H. Owen [a], Piper A. Rawding [a], Caroline M. Hopkins [a], DaWon Kim [a], Daniel J. George [d,e], Andrew J. Armstrong [d,e], Petr Král [c,l], Andrew Z. Wang [f,m], Justine Bruce [g,h], Tian Zhang [d,e,k], Randall J. Kimple [g,h], Seungpyo Hong [a,h,i,j,*]

[a] Pharmaceutical Sciences Division and Wisconsin Center for NanoBioSystems (WisCNano), School of Pharmacy, University of Wisconsin – Madison, 777 Highland Ave, Madison, WI, 53705, USA
[b] Department of Biological Sciences and Bioengineering, Inha University, 100 Inha-ro, Michuhol-gu, Incheon, 22212, Republic of Korea
[c] Department of Chemistry, University of Illinois at Chicago, 845 W Taylor St, Chicago, IL, 60607, USA
[d] Department of Medicine, Division of Medical Oncology, Duke Cancer Institute, Duke University, Durham, 10 Bryan Searle Drive, Durham, NC, 27710, USA
[e] Duke Cancer Institute Center for Prostate and Urologic Cancers, Duke University, 20 Duke Medicine Cir, Durham, NC, 27710, USA
[f] Department of Radiation Oncology, University of North Carolina at Chapel Hill, Chapel Hill, NC, 27599, USA
[g] Department of Human Oncology, University of Wisconsin-Madison, Madison, 600 Highland Ave, WI, 53792, USA
[h] UW Carbone Cancer Center, University of Wisconsin-Madison, Madison, 600 Highland Ave, WI, 53792, USA
[i] Department of Biomedical Engineering, The University of Wisconsin-Madison, 1550 Engineering Dr., Madison, WI, 53705, USA
[j] Yonsei Frontier Lab, Department of Pharmacy, Yonsei University, 50 Yonsei-ro, Seodaemun-gu, Seoul, 03722, Republic of Korea
[k] Department of Internal Medicine and Simmons Comprehensive Cancer Center, University of Texas Southwestern Medical Center, Dallas, TX, 75390, USA
[l] Department of Physics, Department of Pharmaceutical Sciences, University of Illinois at Chicago, 845 W Taylar St, Chicage, IL, 60607, USA
[m] Department of Radiation Oncology and Simmons Comprehensive Cancer Center, University of Texas Southwestern Medical Center, Dallas, TX, 75390, USA

ARTICLE INFO

Keywords:
Bimodal liquid biopsy
Peptide engineering
Cancer immunotherapy
Circulating tumor cells
Exosomes

ABSTRACT

Despite its high potential, PD-L1 expressed by tumors has not been successfully utilized as a biomarker for estimating treatment responses to immunotherapy. Circulating tumor cells (CTCs) and tumor-derived exosomes that express PD-L1 can potentially be used as biomarkers; however, currently available assays lack clinically significant sensitivity and specificity. Here, a novel peptide-based capture surface is developed to effectively isolate PD-L1-expressing CTCs and exosomes from human blood. For the effective targeting of PD-L1, this study integrates peptide engineering strategies to enhance the binding strength and specificity of a β-hairpin peptide derived from PD-1 (pPD-1). Specifically, this study examines the effect of poly(ethylene glycol) spacers, the secondary peptide structure, and modification of peptide sequences (e.g., removal of biologically redundant amino acid residues) on capture efficiency. The optimized pPD-1 configuration captures PD-L1-expressing tumor cells and tumor-derived exosomes with 1.5-fold ($p = 0.016$) and 1.2-fold ($p = 0.037$) higher efficiencies, respectively, than their whole antibody counterpart (aPD-L1). This enhanced efficiency is translated into more clinically significant detection of CTCs (1.9-fold increase; $p = 0.035$) and exosomes (1.5-fold increase; $p = 0.047$) from patients' baseline samples, demonstrating stronger correlation with patients' treatment responses. Additionally, we confirmed that the clinical accuracy of our system can be further improved by co-analyzing the two biomarkers (bimodal CTC/exosome analysis). These data demonstrate that pPD-1-based capture is a promising approach for capturing PD-L1-expressing CTCs and exosomes, which can be used as a reliable biomarker for cancer immunotherapy.

* Corresponding author. Pharmaceutical Sciences Division and Wisconsin Center for NanoBioSystems (WisCNano), School of Pharmacy, University of Wisconsin – Madison, 777 Highland Ave, Madison, WI, 53705, USA.
E-mail address: seungpyo.hong@wisc.edu (S. Hong).
[1] Jiyoon Bu and Woo-jin Jeong contributed equally to this work.

https://doi.org/10.1016/j.bios.2022.114445
Received 19 March 2022; Received in revised form 13 May 2022; Accepted 30 May 2022
Available online 1 June 2022

1. Introduction

For the past decade, immunotherapy targeting checkpoint inhibitors (ICIs), such as programmed death 1 (PD-1) on T cells and its ligand (PD-L1) on cancer cells, has been clinically attempted for the treatment of tumors (Bu et al., 2020a; Pardoll, 2012; Ribas and Wolchok, 2018). Although these PD-1/PD-L1 antagonists demonstrated durable responses in multiple tumor types, the therapy has been shown to be effective in only 10–40% of patients (Borghaei et al., 2015; Ferris et al., 2016; Kowanetz et al., 2018). Due to this inconsistency, there has been an urgent need for a biomarker enabling clinically reliable prediction and monitoring of treatment responses. Based on the clinical data reported to date, PD-L1 expression in tumors is considered to be a good predictive biomarker and has already been utilized for estimating the therapeutic responses to immunotherapies targeting PD-1/PD-L1 pathways (Halse et al., 2018; Kerr, 2018; Yu et al., 2016). For example, PD-L1 expression was found to be closely associated with the efficacy of PD-1/PD-L1 antagonists in non-small-cell lung carcinoma (NSCLC) patients (Abdel-Rahman, 2016).

Despite its potential as a biomarker, the current analysis of tumor PD-L1 has inherent drawbacks. Immunohistochemistry (IHC) of PD-L1 in biopsy specimens, which is the current gold standard, may underrepresent the molecular heterogeneity of a tumor, since this method assesses PD-L1 expression only in a small fragment of tumor obtained at a single time point (Ulrich and Guibert, 2018). As an alternative, liquid biopsy has emerged as an effective real-time monitoring technique for the surveillance of the therapeutic response and tumor progression (Bu et al., 2017a). This technique detects tumoral components in circulation that leak into the vasculature from different subclonal origins at multiple timepoints, tracking the dynamic changes in the entire tumor microenvironment over the course of therapy (Bu et al., 2017b; Esposito et al., 2016). Specifically, liquid biopsy could be a more attractive option for monitoring the response to immunotherapy than the response to other therapeutic approaches. As the majority of tumoral components in the circulation are eliminated by immune cell attack (Steinert et al., 2014), components overexpressing PD-L1 may survive longer in the circulation. Thus, many attempts have been made to estimate PD-L1 expression in a tumor based on liquid biopsy (Anantharaman et al., 2016; Kulasinghe et al., 2017; Mazel et al., 2015; Oliveira-Costa et al., 2015; Xu et al., 2019; Yue et al., 2018). These studies demonstrated the potential clinical use of liquid biopsy systems to help monitor patients' responses to immunotherapy.

To date, antibodies have been the most frequently utilized capture agent for the isolation of tumoral components in liquid biopsy, owing to their high affinity and selectivity toward specific cancer-associated proteins. However, their low thermodynamic stability and high manufacturing cost limit their rapid clinical translation (Leader et al., 2008). Furthermore, antibodies are composed of many different functional groups (e.g., amine, carboxyl, and sulfhydryl groups) that may nonspecifically interact with any biological substance. Due to these hurdles, current antibody-based assays lack the sensitivity and specificity needed for high clinical utility. To overcome these issues, peptides have been investigated as an alternative capture agent to antibodies, given their unique advantage of being molecularly intermediate between small molecules and proteins (Lau and Dunn, 2018). The primary structure and molecular topology of peptides can be easily and precisely manipulated using a solid-phase synthesis method (conjugating amino acids one at a time) (Jeong et al., 2014). This modular property allows peptides to be immobilized on a substrate in a controlled density, orientation, and conformation, which can maximize their individual binding strength that can be further enhanced by the multivalent binding effect (Sargeant et al., 2008; Xiong et al., 2017).

In this study, we developed a multimodal liquid biopsy system based on PD-L1-binding peptides to effectively detect tumoral components of different sizes, such as PD-L1-expressing circulating tumor cells (CTCs) and exosomes, in circulation. We previously demonstrated that the β-hairpin peptide isolated from an engineered PD-1 protein (pPD-1) strongly binds to PD-L1 when the peptides are conformationally stabilized via conjugation to nanoparticles (Jeong et al., 2020). To use pPD-1 as a capture agent for tumor biomarkers, we employed three peptide engineering strategies to maximize its capture sensitivity and specificity toward PD-L1-expressing CTCs and exosomes (Fig. 1). First, pPD-1 was attached to a glass substrate through poly(ethylene glycol) (PEG; 5 kDa) linkers to exploit the nonfouling properties of PEG. However, our previous results demonstrated that the stabilization of the pPD-1 hairpin structure was partially attributed to intermolecular forces between the peptide andnanoparticle (Jeong et al., 2020). Due to the presence of the linker, these interactions cannot be utilized in the pPD-1-PEG configuration. Hence, as the second engineering approach, we varied the PEGylation site in the peptide (in the strand region, pPD-1S; in the turn region, pPD-1T), assuming that the similarity in molecular symmetry would increase the propensity for β-hairpin formation (bilateral symmetry). Third, PD-1 core-forming amino acid residues (CAARs) that are unnecessary for PD-L1 binding were substituted with glycine to further reduce nonspecific interactions (generating pPD-1G). After optimization, the *in vitro* efficiency and clinical translatability of the surface-immobilized peptides (pPD-1G-PEG) were validated and compared to those of an anti-PD-L1 antibody (aPD-L1). Furthermore, bimodal analysis of CTCs and exosomes was conducted to enhance the clinical accuracy of our peptide-based liquid biopsy system. Specifically, both CTCs and exosomes were isolated from the identical patients using our system, and the expression profiles of the two biomarkers were coanalyzed to further increase the diagnostic capability. The bimodal analysis results were compared to those obtained from either of the tumor biomarkers alone. The results presented in this study provide novel peptide engineering strategies that could be applied for the isolation of various PD-L1-expressing biomarkers, allowing the development of a reliable bimodal liquid biopsy system for monitoring treatment responses to immunotherapy.

2. Materials and methods

2.1. Materials

Fmoc-amino acids and coupling reagents were purchased from either Anaspec (Fremont, CA) or Novabiochem (Germany). PEG (NH2-(PEG)-COOH, 5 kDa) were purchased from Nektar Therapeutics (Huntsville, AL). CellTracker Green was obtained from Thermo Fisher Scientific (Waltham, MA). Fetal bovine serum (FBS) and antibiotic mixture (penicillin/streptomycin; P/S) were acquired from Invitrogen. Dulbecco's modification of Eagle's medium (DMEM), Eagle's minimum essential medium (EMEM), Roswell Park Memorial Institute (RPMI) medium, Leibovitz's L-15 medium, and 0.25% trypsin EDTA were purchased from Corning (Manassas, VA). All cell lines were obtained from American Type Culture Collection (Manassas, VA). aPD-L1 was obtained from BioXcell (West Lebanon, NH) and R&D systems (goat anti-human; for staining the cells; Minneapolis, MN). Recombinant human PD-L1 protein was purchased from R&D Systems. For immunohistochemistry, rabbit antibody against human pan-cytokeratin (CK; 1:50, Abcam 9377), AlexaFluor 647-conjugated secondary antibody against anti-rabbit (1:100, Invitrogen), mouse antibody against human CD45 (1:500, BD Biosciences 555480), AlexaFluor 488-conjugated secondary antibody against anti-mouse (1:100, Invitrogen), AlexaFluor 488-conjugated secondary antibody against anti-goat (Invitrogen), and 4′,6-diamidino-2-phenylindole (DAPI)-included mounting media (VectaShield Laboratories, Inc.) were utilized. All other chemicals were obtained from Sigma-Aldrich (St. Louis, MO), unless otherwise stated.

2.2. Peptide synthesis

Rink Amide MBHA resin LL or 2-Chlorotrityl chloride resin (Novabiochem, Germany) were utilized as a scaffold for peptide synthesis.

Peptide sequences were synthesized based on standard Fmoc chemistry, as described previously.[26] Resin-bound peptides were treated for 2 h with a cleavage cocktail which consists of a mixture of trifluoroacetic acid (TFA), thioanisole, and ethanedithiol (EDT) at a ratio of 95: 2.5: 2.5 (2 mL) at room temperature, followed by precipitation using tert-butyl methyl ether. The reverse-phase high performance liquid chromatography (HPLC) was utilized to purify the resulting peptides (room temperature; mobile phase of water/acetonitrile with 0.1% TFA). The molecular weight of the final product was determined using Matrix-assisted laser desorption/ionization time-of-flight (MALDI-TOF) mass spectrometry (AXIMA, Shimadzu, Japan) with α-Cyano-4-hydroxycinnamic acid (CHCA) matrix. The peptide concentration of the final product was then quantitatively measured using an ultraviolet–visible (UV–Vis) spectrophotometer.

2.3. Surface preparation

Schematic diagrams of the surface preparation process are provided in Fig. S1-**S4**. To immobilize the peptides onto the surface, polydimethylsiloxane (PDMS) gaskets having three separate wells of 20 mm × 10 mm were utilized for the surface treatments on epoxy-functionalized slides (Tekdon, Myakka City, FL). PEG or glycine linkers were treated on each well at a concentration of 200 μM in ddH_2O. The wells were rinsed and carboxyl groups of the PEG (or glycine) linkers were activated for 1h with 50 mM 1-ethyl-3-(3-dimethylaminopropyl)carbodiimide hydrochloride (EDC) and 100 mM N-hydroxysuccinimide (NHS). The surfaces were then incubated overnight with an excessive amount of peptide (300 μM) or antibody (0.7 μM). The peptide (or antibody)-functionalized slides were either loaded into a flow chamber and used for cell retention measurement or directly used for exosome capture with three-well PDMS gaskets (Fig. S1-**S4**).

E-selectin was coated on an epoxide glass slide, in between the peptide (or antibody)-functionalized regions, to induce cell rolling. After immobilizing the capture agents (peptides or antibodies), three-well PDMS gaskets were replaced with one-well PDMS gaskets. The surface was then incubated with E-selectin (60 nM in PBS) for 4 h at RT. The slides were assembled with the flow chambers (Fig. S1-**S4**) and used for CTC capture.

2.4. Force spectroscopy measurement using Atomic Forc Microscopy (AFM)

For the probe functionalization, PNP-TR-Au-30 AFM probes (Nano World) were treated with a mixture of 1.9 mg/mL 5 kDa methoxyPEG-thiol and 0.1 mg/mL 7.5 kDa carboxyl-PEG-thiol (Jenkem) in ddH_2O. The probes were washed with ddH_2O, NHS-activated for 1 h, and reacted with recombinant PD-L1 overnight. The spring constants of the probes were determined by the thermal noise method.

The PD-L1 binding strength of the synthesized peptides was analyzed by measuring the rupture forces using AFM. Specifically, rupture forces between probe-immobilized PD-L1 and surface-bound peptides (or antibodies) were recorded using Asylum Infinity Biosystem (Oxford

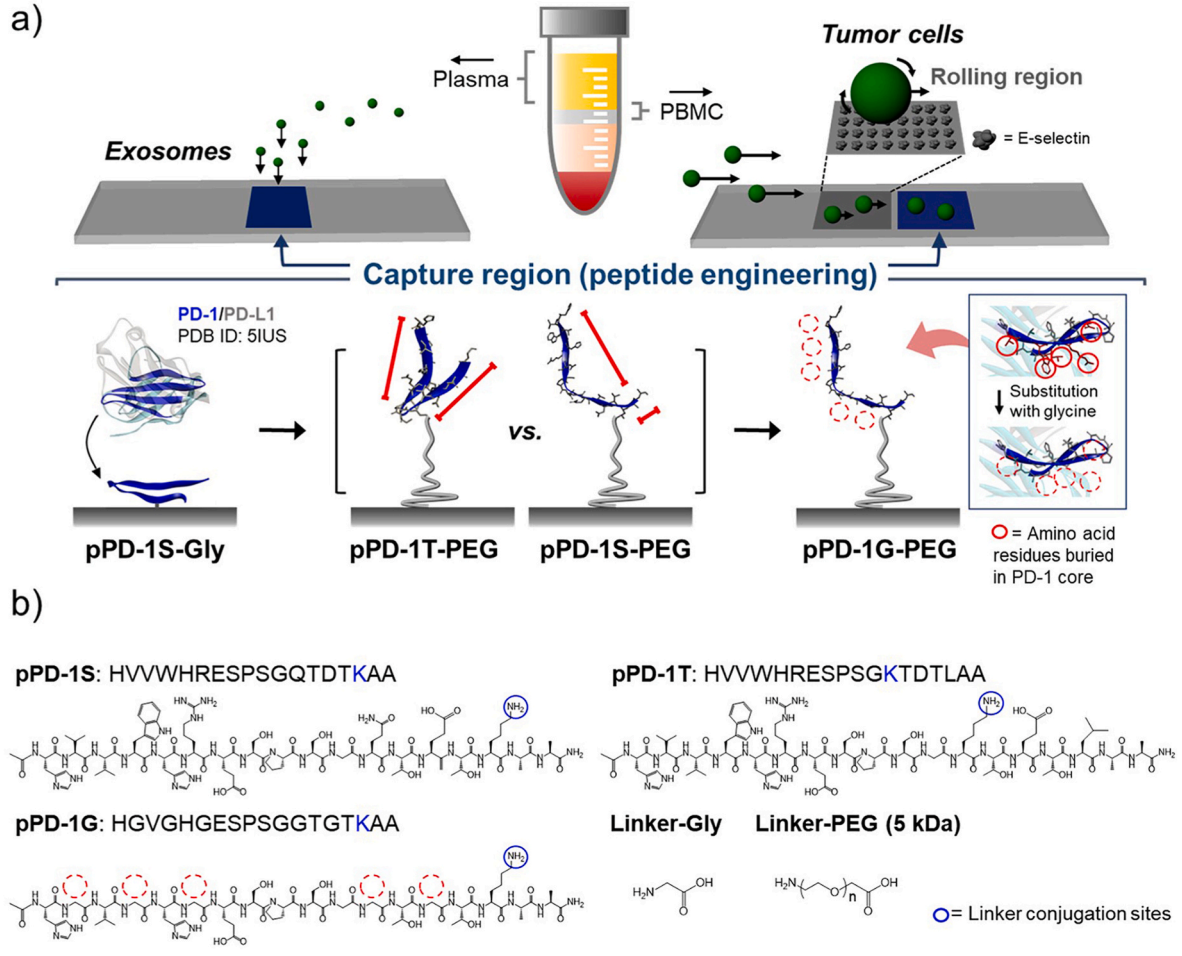

Fig. 1. Overview of the peptide-based bimodal liquid biopsy system. a) Schematic illustration of the capture surfaces for concurrent detection of both CTCs and tumor-derived exosomes. The surfaces are functionalized with engineered peptides that are modified by conjugation of PEG at different sites and via sequence modification to improve the overall capture efficiency. b) Chemical structures of the peptides (pPD-1S, pPD-1T, and pPD-1G) and the linkers (Gly and PEG) used in this study.

Instruments, Santa Barbara, CA). Note that both samples and probes were hydrated with PBS solution. The AFM force spectroscopy was conducted at a force-cycle consisting of a 2 μm approach at 2 μm/s, dwell time of 1 s, and retraction at 0.5, 1, 2, 5, 10, and 20 μm/s. Based on the force-distance (FD) curves obtained from the AFM, the average rupture forces were calculated at each retraction velocity. These forces were then fitted to the modified Bell-Evans model (Poellmann et al., 2020) to obtain PD-L1 dissociation rates (k_d) of different peptide-immobilized surfaces. The binding strengths were then compared based on the rupture forces at each retraction velocity and the dissociation rate with PD-L1 protein.

AFM adhesion force mapping was conducted in the desired area of 10 μm square. Briefly, 32 × 32 array of FD curves were obtained from pPD-1G-PEG or aPD-L1-PEG surfaces using a probe functionalize with PD-L1 proteins which had a spring constant of ~59 pN/nm. The force cycle consisted of a 2 μm approach at 2 μm/s, 1 s dwell time, and retraction at 2 μm/s. The number of discrete unbinding events for each FD curve was identified by counting the abrupt changes in unloading forces which were greater than 150 pN. Note that the threshold was set as 150 pN, which is > 20 times greater than the root-mean-square (rms) noise signal from the probe. The maximum adhesion force and energy of adhesion between the probe and surface were also obtained from each FD curve and mapped into a 2D plane of 32 × 32 pixels.

2.5. Cell culture and labelling

Two human breast cancer cell lines (MDA-MB-231 and MCF-7), two human renal cell carcinoma (RCC) cancer cell lines (786-O and ACHN), and one human leukemia cell line (Jurkat) were used in this study. MDA-MB-231 cells, MCF-7 cells, and ACHN cells were cultured in Leibovitz's L-15 medium, DMEM, and EMEM, respectively, supplemented with 10% (v/v) FBS and 1% (v/v) P/S. 786-O cells and Jurkat cells were grown in RPMI medium supplemented with 10% FBS and 1% P/S. MDA-MB-231 cells were grown in atmospheric air at 37 °C. All other cell lines were cultured in a controlled humidified atmosphere with 5% CO_2 at 37 °C. Cancer cells were grown as a monolayer, while Jurkat cells were cultured in suspension. Cells were grown in either T-25 (for cell retention/capture experiments) or T175 flasks (for collecting exosomes) until they reach 60–80% confluency.

For the cell labelling, cells were gently washed with PBS solution three times and harvested from a cell culture flask by treating 0.25% trypsin EDTA, followed by centrifugation at 300*g* for 5 min. Jurkat cells were collected directly from the cell culture medium without trypsin. Cells were then incubated for 15 min in 1 mL complete DMEM medium (with 10% FBS and 1% P/S) containing 5 μM CellTracker green dye (Invitrogen) per 5×10^5 cells. Cells were centrifuged at 300 g for 5 min and resuspended in 3 mL complete DMEM medium. The centrifugation was repeated three times to wash out the remaining fluorescent dye.

2.6. Molecular dynamics (MD) simulation

The pPD-1S-PEG and pPD-1T-PEG peptides and their target molecules on PD-L1 proteins were simulated in physiological solutions (0.15 M NaCl in water solvent) by NAMD2 using the CHARMM36 protein force field (MacKerell et al., 1998; Phillips et al., 2005). The particle mesh Ewald (PME) method was applied to describe long-range Coulombic coupling. The time interval of 2 fs was used in the simulation (Jarvis et al., 2015). The simulation was performed using Langevin dynamics with a damping constant of 1 ps^{-1} in the isothermal-isobar ensemble (NPT) at a temperature of 310 K and a pressure of 1 bar. The PD-L1 protein was restrained through the whole simulation using harmonic forces with a spring constant of 2 kcal/(mol $Å^2$). To calculate the average retention times and binding energy, we repeated the simulation 3 times for each PD-L1/peptide complex, where each simulation lasted 200 ns.

Binding energies between PD-L1 and the peptides were calculated by the NAMD energy plugin. Briefly, the residues interacting with PD-L1 were determined by 5 Å cutoff distance and verified by visualization (for the simulation with longer retention time). The electrostatic and vdW energy contributions between two interacting pieces were calculated by the NAMD energy plugin. The electrostatic contribution was given as equation (1),

$$U_{elec} = \sum_{i=1}^{n} \sum_{j>i}^{n} \frac{1}{4\pi\varepsilon} \frac{q_i\, q_j}{\left|\vec{r}_i - \vec{r}_j\right|}, \quad (1)$$

where $|ri\rightarrow - rj\rightarrow|$ is the distance between two charges, q_i, q_j, and ε are the dielectric constant of the solvent that was set to 78.65 78.5 in energy calculations. Long-range electrostatic interactions were calculated by the PME method.

The vdW interactions and close distance atomic repulsions were described by the Lennard-Jones (LJ) 6–12 potential energies,

$$U_{LJ} = \sum_{i=1}^{n} \sum_{j>i}^{n} \varepsilon_{ij} \left[\left(\frac{\sigma_{ij}}{r_{ij}}\right)^{12} - \left(\frac{\sigma_{ij}}{r_{ij}}\right)^{6} \right], \quad (2)$$

where ε_{ij} is the maximum of the stabilization energy for the ith and the jth atoms, σ_{ij} is the distance between ith and jth atoms at the minimum potential, and r_{ij} is the actual distance between two atoms. The LJ parameters between different atom types were calculated using $\sigma_{ij} = (\sigma_{ii} + \sigma_{jj})/2$ and $\varepsilon_{ij} = \varepsilon_{ii}\, \varepsilon_{jj}$ as a mixing rule (Lorentz Berthelot rules).

2.7. Peripheral blood mononuclear cells (PBMC) and plasma separation

Human blood samples were obtained from Duke University Hospital (study #Pro0076768) and the University of Wisconsin-Madison (study #UW17078, #UW18098, and #2016–1555) according to protocols approved by the institutional review board (IRB) at each institute. Informed written consent was obtained from all participating subjects. PBMC and plasma layers were separated from 4 mL human whole blood using Ficoll-Paque® Plus (Cytiva, Marlborough, MA) density gradient centrifugation. Specifically, the whole blood was diluted with PBS solution at a 1:1 ratio and the diluted blood sample was gently laid above 4 mL Ficoll-Paque® Plus. Samples were then centrifuged at room temperature at 1500 g for 20 min with the brakes off. Plasma and PBMC layers were separately collected. The remaining large debris was depleted from the plasma by two-step centrifugation at 750*g* for 10 min. For PBMC layers, the supernatants were aspirated after centrifugation at 750*g* for 10 min (twice), and the remaining PMBCs were contained in 100 μL PBS solution. Note that 1 mL of human blood was used for the samples obtained from the University of Wisconsin-Madison.

2.8. In vitro flow chamber cell retention assay

The peptide-functionalized slides were housed using flow chambers (Fig. S2-**S4**). The fluorescent-labeled cells were infused through the flow chamber at a maximum shear stress of 3.6 dyne/cm^2 (5 mL/min) using a syringe pump (New Era pump 505 Systems Inc., Farmingdale, NY). Cells were incubated for 30 min at room temperature. Cell retention (retention efficiency) was determined as the ratio of the cells retained on the surface upon 20 min washing at a maximum shear stress of 0.36, 3.6, and 36 dyne/cm^2. The PD-L1 binding specificity of the peptide (or antibody)-immobilized surfaces was obtained by comparing the retention efficiency of PD-L1^{High} 786-O cells and PD-L1^{Negative} Jurkat T cells on each surface. The surface that has a high retention efficiency for 786-O cells and low retention efficiency for Jurkat T cells was considered to have a high *in vitro* specificity towards PD-L1.

The flow chamber cell retention assay was also utilized to compare the stability of the pPD-1G-PEG and aPD-L1-PEG surfaces against serum, thermal stress, and enzymatic degradation. Prior to the cell retention assay, either the aPD-L1-PEG or pPD-1G-PEG surface was incubated

with i) 10% fetal bovine serum (FBS) or ii) 1:1 diluted human serum in PBS solution for 20 min to test the serum stability. Thermodynamic stability was examined by incubating the capture surfaces at iii) 80 °C for 20 min. The stability against enzymatic degradation was tested by treating the peptide- or antibody-functionalized glass slides with either iv) 0.1 mg/mL proteinase K or v) 0.25% trypsin-EDTA at either room temperature (RT) or 37 °C.

2.9. CTC/cancer cell capture

The complete cell capture slides, consisting of capture regions with either PD-L1-targeting peptides or antibodies and E-Selectin-functionalized cell rolling regions in between the capture regions, were loaded into a flow chamber (Fig. S2-**S4**). PBMC layers or cell suspensions were withdrawn through the flow channels in a chamber at 0.36 dyne/cm^2 for 20 min. The captured cells were incubated in a flow chamber for 5 min and washed in a reverse direction at twice the capture flow rate (0.72 dyne/cm^2) for 20 min. For CTC analysis, capture slides were gently disassembled from the flow chamber and co-stained with CK (red), CD45 (green), and DAPI (blue), as described in our previous publication.[25] For *in vitro* samples, capture efficiency was determined as the ratio of the cells captured on the surface compared to their initial count, which was approximately 2500 cells/test (7500 cells/test when analyzing the spatial distribution of the captured cancer cells).

2.10. Western blot analysis

The cells were pelleted at 300×*g* for 3 min and lyses using RIPA buffer with sonication. The lysates were centrifuged at 20,000×*g* for 10 min at 4 °C and the supernatant was collected. The amount of protein on the supernatant was quantified using BCA assay (Pierce™ BCA Protein Assay Kit, Thermo Fisher Scientific, Waltham, MA). A total of 20 μg proteins were separated on SDS-PAGE, followed by transfer to PVDF membrane in wet transfer condition. The PVDF membrane was blocked with skim milk for 1 h at RT, followed by incubating with the primary antibody against PD-L1 (Polyclonal anti-PD-L1, NBP2-15791, Novus Biologicals) for 12 h at 4 °C. The membrane was then treated with HRP (horse Radish Peroxidase)-conjugated secondary antibody (R&D Systems) for 1 h at room temperature. β-actin (monoclonal anti-β-Actin, MAB8929, R&D Systems) was used as a loading control. The labeled proteins were visualized with Syngene G:Box F3 (Syngene, Frederick, MD) with Clarity Western ECL Substrate (Bio-Rad, Hercules, CA) chemiluminescent reagent.

2.11. In vitro exosome sample preparation

Cell culture medium was replaced with serum-free medium containing 1 wt% bovine serum albumin (BSA), after cells reached 60–80% confluency. Note that the serum-free medium was filtered twice with a 0.22 μm vacuum filter (Millipore, Bedford, MA), prior to the incubation. Cell culture medium was collected after 36 h cell culture in T-175 flasks, and the centrifugation was carried out sequentially at 300 g and 12,000 g to remove the cells and other large cellular debris. Cell medium was then ultracentrifuged at 120,000 g using a Beckman type 45Ti rotor and the supernatants were gently removed. Exosomes were resuspended in PBS solution and their concentration was determined using NTA.

2.12. Exosome capture and analysis

In vitro cell-derived exosomes (2 × 10^8 vesicles/mL) or plasma samples were incubated for 3 h on either pPD-1G-PEG, aPD-L1-PEG, or PEGylated slides covered with three-well PDMS gaskets (2 μL/mm^2). The wells were then washed with 400 μL PBS solution for three times. The amount of exosome captured on each surface was quantitatively measured using either NTA, BCA protein assay, DiO membrane staining assay, or surface roughness measurement.

2.13. Nanoparticle tracking analysis (NTA)

The concentration and size of exosomes were determined using NTA (Malvern Nanosight NS300). Samples were obtained before and after treating them on either pPD-1G-PEG, aPD-L1-PEG, or PEGylated slide. Three 60s-long videos were taken for each sample in a flow mode at a speed of 70 Au. The minimum track length and detection threshold was set as 10 and 5, respectively, with sample viscosity set to the corresponding viscosity to PBS solution at 25 °C. The analysis was performed in duplicates for the clinical samples and triplicates for *in vitro* cell-derived samples.

2.14. Exosome labeling

Exosomes captured on either of pPD-1G-PEG, aPD-L1-PEG, or PEGylated surfaces were treated 15 min with 5 μg/mL Vybrant DiO (Thermo) at 37 °C. Wells were gently washed with 400 μL PBS solution three times. The slides were then placed above the inverted fluorescent microscope and the tiled images were scanned at 5 × magnification. Images of each well were collected with consistent exposure time, and brightness and contrast of images were also manipulated consistently across the samples. Images were extracted in JPEG format and fluorescent intensity was quantified using Image J software.

2.15. Surface roughness measurement

Height profiles of different exosome capture surfaces were collected with silicon probes (OLYMPUS AC160TS-R3) with a resonant frequency of 300 kHz and a spring constant of 26 N/m, using an Asylum MFP-3D Infinity Biosystem (Oxford Instruments, Santa Barbara, CA). The roughness of each surface was quantitatively analyzed from the average root mean square (Rq) of three independent 10 μm × 10 μm square images.

3. Results

3.1. PEG linkers reduce nonspecific protein adsorption

Glycine linkers were employed to conjugate pPD-1 peptides to an epoxy-functionalized glass substrate, considering that these short linkers would allow the peptides to directly interact with the substrate and induce β-hairpin stabilization (pPD-1S-gly, Figs. 1 and S1). An *in vitro* flow chamber retention assay (Fig. S2-S4) was conducted using PD-L1^{High} 786-O cells to assess the binding specificity of pPD-1S-gly to PD-L1-expressing biomolecules. As demonstrated in Fig. S5, 99.2 ± 3.6% of the surface-adhered 786-O cells were retained on the surface after 30 min of incubation followed by 20 min of washing at 0.36 dyne/cm^2. However, there were significant nonspecific interactions found at the surface, as ~17% of PD-L1^{Negative} Jurkat cells also were retained on the surface, presumably due to their interaction with epoxide groups on the substrate. To address this, we replaced the glycine linkers with 5 kDa PEG molecules (pPD-1S-PEG). PEG, one of the most frequently used linkers for preventing undesired biological interactions (Charles et al., 2009; Hsu et al., 2014), was utilized as a spacer between the substrate and peptides to prevent nonspecific protein adsorption and reduce the binding of PD-L1^{negative} biomolecules. As shown in Figs. S5 and S6, the pPD-1S-PEG surface showed a similar level of 786-O cell retention to that of pPD-1S-gly (96.7 ± 3.8%; p = 0.383) while demonstrating less adhesion to Jurkat cells (10.2 ± 2.9%; p = 0.051). However, this structure spatially segregates the pPD-1S peptides from the substrate and hinders intermolecular peptide–substrate interactions, which may affect the binding strength of the peptide to PD-L1. This potential limitation led us to explore additional hairpin stabilization strategies that are compatible with PEG linkers.

3.2. Peptide symmetry controls β-hairpin folding and binding properties

We synthesized two pPD-1 peptides having different PEG conjugation sites, one at the middle of one of the two strands (pPD-1S-PEG) and another near the turn region (pPD-1T-PEG; Fig. 1). We hypothesized that β-hairpin formation would be improved due to the bilateral symmetry of the peptides when they were conjugated to PEG near the elbow region (pPD-1T-PEG). Peptides were conjugated to PEGylated microbeads, and circular dichroism (CD) spectroscopy was utilized to investigate the peptide folding structure. Conjugation of pPD-1S peptides to the PEGylated microbeads did not alter their random coil structure, as indicated by the strong negative band at 200 nm (Jeong et al., 2022; Waqas et al., 2017). In contrast, pPD-1T exhibited partial β-hairpin folding after conjugation, as shown by the weak shoulder at 214 nm (Fig. 2a). (Jeong et al., 2020)

To further evaluate the folding properties, we compared the binding kinetics of the two peptide structures using AFM. Interactions between probe-immobilized PD-L1 and surface-immobilized peptides were recorded at different pulling velocities (0.5–20 μm/s), and the data were then fitted to the modified Bell-Evans model (Friddle et al., 2012). Folded peptides are known to exhibit slower dissociation than unstructured peptides, although the exact mechanism is not fully understood (Miles et al., 2016; Rogers et al. 2014a, 2014b). Despite the incomplete β-hairpin formation, a similar trend was observed for pPD-1 peptides. As shown in Figs. 2b and S7, partially folded pPD-1T-PEG exhibited stronger binding to PD-L1 than the unstructured pPD-1S-PEG, resulting in an ~5-fold enhancement in off-rate kinetics ($2.19 \times 10^2\ s^{-1}$ vs. $10.56 \times 10^2\ s^{-1}$). The atomistic molecular dynamics (MD) simulation supported this observation (Fig. 2c).(Cagno et al., 2018; Han and Král, 2020; Sen et al., 2018) The MD simulation showed average retention times of ~75 ns and ~25 ns and binding free energies of −19.42 kcal/mol and −9.24 kcal/mol for pPD-1T-PEG and pPD-1S-PEG, respectively, toward PD-L1 proteins. The simulation also revealed that when interacting with the PD-L1 protein, the LYS/PEG residue located in the hairpin turn of pPD-1T pulls the peptide symmetrically and helps the peptide form a stable binding interaction with PD-L1, whereas the LYS/PEG residue in pPD-1S pulls one sheet of the peptide and deforms the β-hairpin structure (Videos S1 and S2). The secondary structure-dependent off-rate binding kinetics were further confirmed using a cell retention assay (Figs. 3a and S8). Under low and moderate shear stresses (0.36 and 3.6 dyne/cm^2, respectively), the retention of 786-O cells was >90% for both configurations. However, at a higher shear stress (36 dyne/cm^2), >95% of the cells were detached from the pPD-1S-PEG surface, whereas 21.5 ± 3.0% of cells remained adhered to the pPD-1T-PEG surface ($p = 0.051$).

Supplementary data related to this article can be found at https://doi.org/10.1016/j.bios.2022.114445.

Next, a cell capture assay was conducted using the same flow chamber, i.e., capture of cancer cells was evaluated under continuous flow conditions. Either pPD-1S-PEG or pPD-1T-PEG was applied to a rolling-based CTC capture system, in which E-selectin immobilized between the peptide-functionalized regions induces cells to roll on a surface, increasing the chance that the cells will interact with the peptides (Figs. S2–S4) (Bu et al., 2020b; Myung et al. 2015, 2018). Unexpectedly, the unstructured pPD-1S surface showed considerably enhanced cell capture compared with the pPD-1T surface (Fig. 3b): the capture efficiencies of pPD-1S-PEG vs. pPD-1T-PEG obtained using 786-O cells were 84.8 ± 13.4% vs. 61.8 ± 10.1% ($p = 0.034$) and 83.9 ± 6.6% vs. 58.0 ± 10.1% ($p = 0.033$) at 0.18 and 0.36 dyne/cm^2, respectively. Analysis of the spatial distribution of the captured cancer cells further supported the

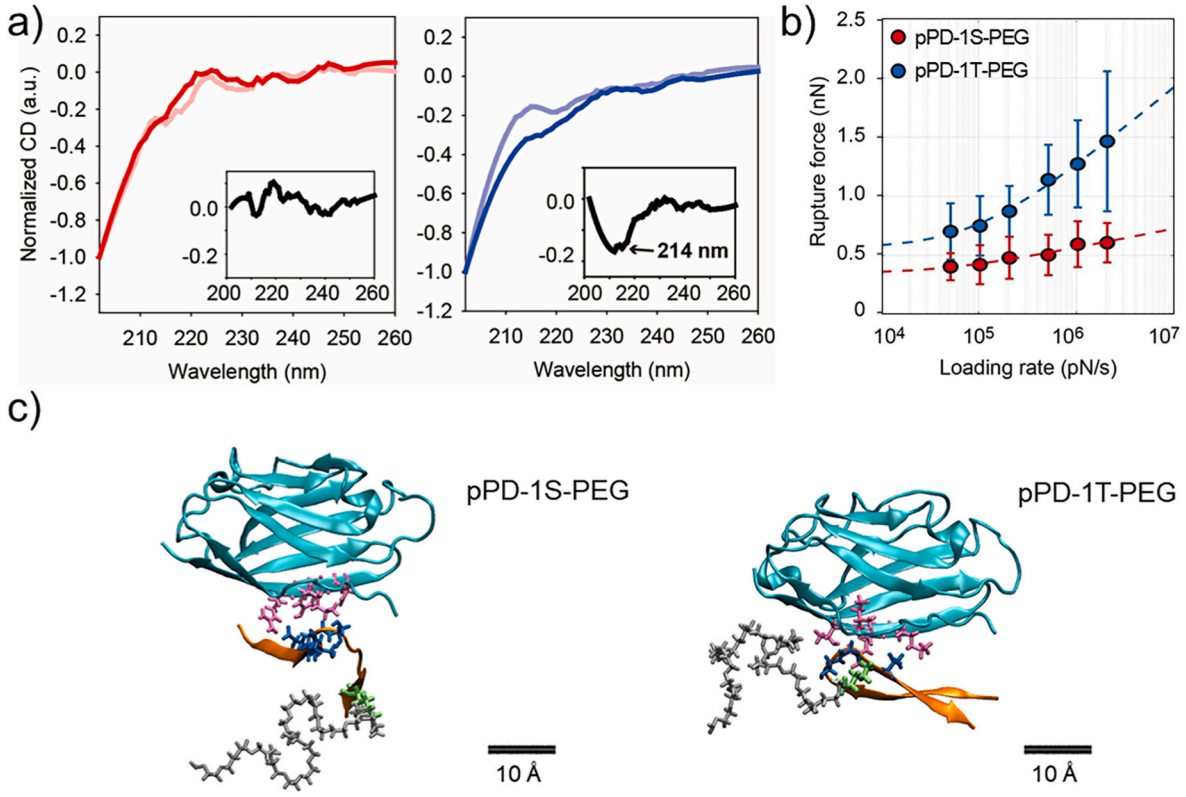

Fig. 2. PEG conjugation site-dependent binding behaviors of pPD-1. a) CD spectra of pPD-1S (left) and pPD-1T (right) in PBS (bright red and blue) or after conjugation with PEGylated microbeads (dark red and dark blue). Insets: difference spectra of the peptides (CD signals from the peptides in PBS minus those from the peptides conjugated to the beads). b) Off-rate binding kinetics of pPD-1S-PEG and pPD-1T-PEG to PD-L1, as measured using AFM, which is based on the force-distance curves fitted to the modified Bell-Evans model. c) Snapshots of MD simulation of pPD-1S-PEG and pPD-1T-PEG coupled to PD-L1. Cyan: PD-L1, pink: binding residues on PD-L1, orange: peptides, blue: binding residues on peptides, silver: PEG, and green: lysine (LYS).

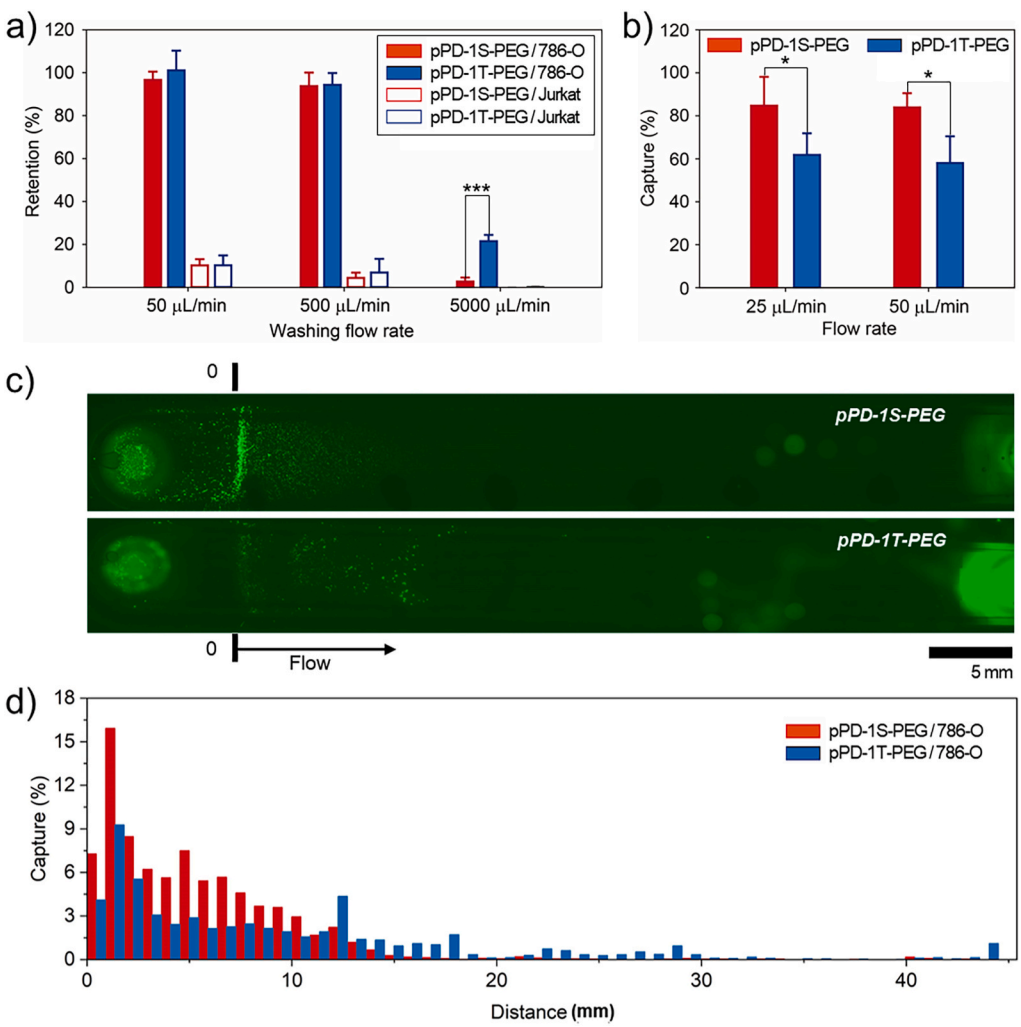

Fig. 3. *In vitro* binding efficiency of pPD-1 peptides depending on the PEG conjugation site. a) *In vitro* cell retention assay results on the pPD-1S-PEG and pPD-1T-PEG surfaces. Cell retention was measured after 20 min washes at maximum shear stresses of 0.36, 3.6, and 36 dyne/cm^2, which correspond to 50, 500, and 5000 μL/min, respectively. b) *In vitro* cell capture assay results on the pPD-1S-PEG and pPD-1T-PEG surfaces at flow rates of 25 and 50 μL/min (0.18 and 0.36 dyne/cm^2, respectively). c, d) Spatial profiles of captured cancer cells on the pPD-1S-PEG and pPD-1T-PEG surfaces at a flow rate of 50 μL/min (0.36 dyne/cm^2). The number of captured cancer cells on the two peptide-immobilized surfaces was analyzed depending on the distance from the inlet.

higher cell capture capability of the pPD-1S-PEG surface, as the majority of 786-O cells were captured near the inlet on the pPD-1S-PEG surface, while the cells were more broadly distributed across the pPD-1T-PEG surface (Fig. 3c and d).

In summary, the relocation of the PEGylation site from the middle of one of the strands (pPD-1S-PEG) to near the turn region (pPD-1T-PEG) induced partial folding of the peptide and was associated with slower dissociation from PD-L1 proteins. However, when utilized for the capture of cancer cells under fast-flow conditions, pPD-1S-PEG showed a significantly stronger cell capture capability. The inconsistency between the cell retention and capture assays could be explained by the 'induced-fit' interaction model, which demonstrates the relationship between the secondary structure of peptides and their binding behaviors. According to this model, preorganized (folded) biomolecules exhibit slow association since their constrained structure limits their 'ways to bind' (entropic disadvantage) while also slowing dissociation (Amaral et al., 2017; Hoffman et al., 2015; Miles et al., 2016). In contrast, the fast association of unfolded peptides is analogous to the 'fly-casting' binding mechanism, i.e., unstructured proteins weakly bind to target molecules via a distal component, and this binding is followed by additional interactions along with conformational stabilization (Shoemaker et al., 2000). The pPD-1 peptide was isolated from an engineered PD-1 ectodomain that exhibited high affinity for PD-L1 due to its optimized amino acid composition (Jeong et al., 2020). The engineered (substituted) amino acid residues included in the pPD-1 peptide would thus be competent for the initial binding interaction, which would be more effective in the peptide with the unstructured conformation (pPD-1S) (Fig. S9). This in turn facilitates the highly sensitive capture of PD-L1-expressing tumor cells under fast-flow conditions.

3.3. Elimination of redundant pPD-1 CAARs enhances selectivity

The CAARs of pPD-1, which have various chemical properties (as polar, acidic, basic, nonpolar, and aromatic amino acids), could induce nonspecific interactions with different biomolecules (Fig. 4a). Hence, we substituted glycine residues for the CAARs that are unnecessary for PD-L1 binding (pPD-1G). Although the multiple glycine substitutions may destabilize the peptide folding structure, our results demonstrated that the unstructured pPD-1S more effectively captured the PD-L1-expressing cells than the partially folded pPD-1T, allowing this strategy to be compatible with our system. As shown in Fig. 4b, glycine substitution did not affect the capture of PD-L1-expressing cancer cells. The capture efficiency of 786-O cells on the pPD-1G-PEG surface was comparable to that on the pPD-1S-PEG surface since no changes were made in the amino acid residues that interact with PD-L1. In contrast, glycine substitution highly reduced the capture of PD-L1^{Negative} Jurkat cells (7.4 ± 2.3% for pPD-1S-PEG vs. 3.2 ± 2.1% for pPD-1G-PEG; $p = 0.039$). To corroborate this result, biolayer interferometry (BLI) was utilized to assess the nonspecific adsorption of bovine serum albumin (BSA) onto pPD-1S and pPD-1G. Probe-conjugated BSA exhibited a stronger interaction with pPD-1S than pPD-1G at a peptide concentration of 400 μM (Fig. 4c).

We also found that the optimized peptide configuration (pPD-1G-PEG) exhibited a substantially higher capture efficiency than did the

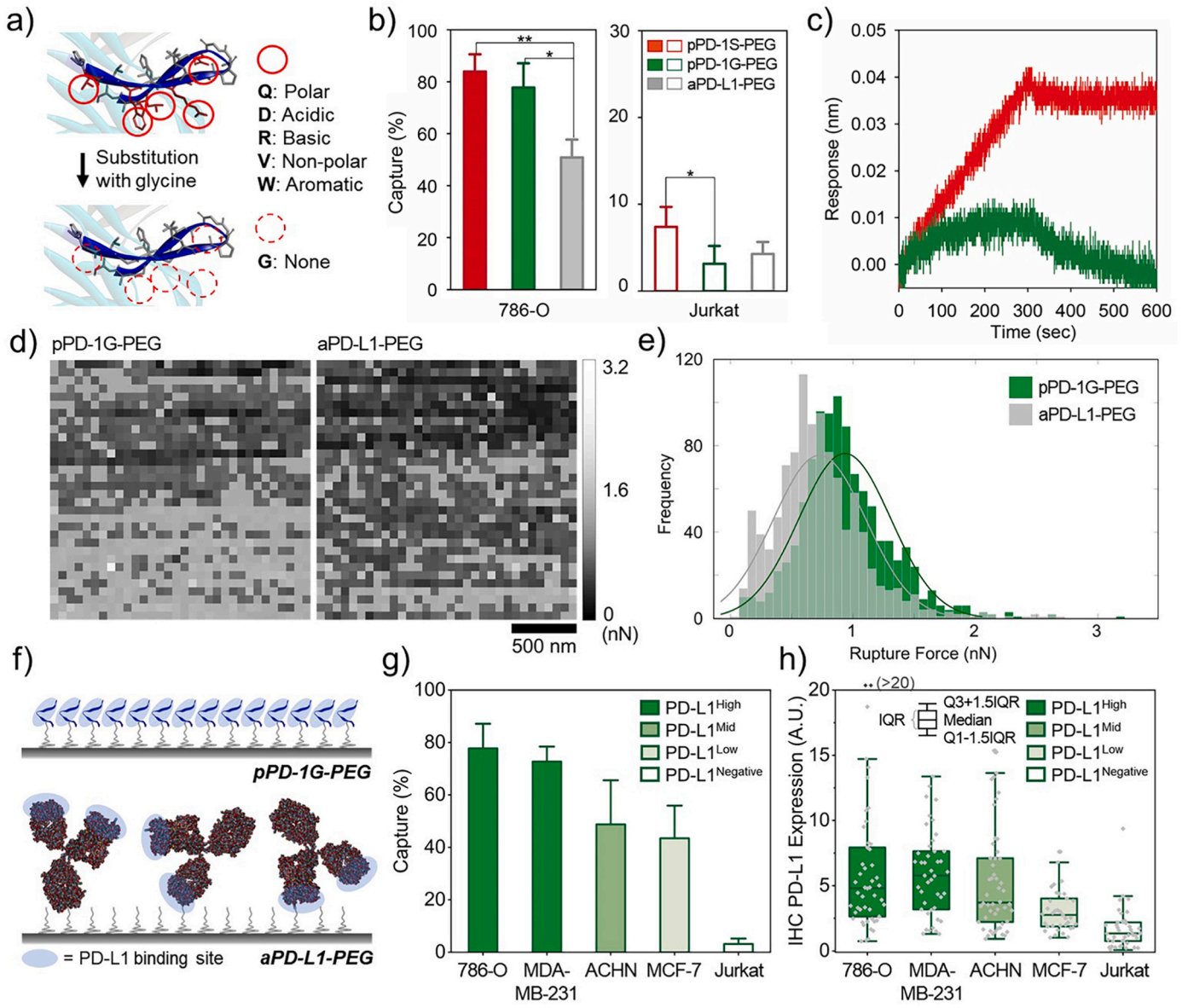

Fig. 4. Engineered pPD-1 peptides (pPD-1G) for effective capture of PD-L1-expressing CTCs: a) Schematic illustration of pPD-1G, in which redundant CAARs in pPD-1S are substituted with glycine residues. b) Cell capture efficiency and selectivity of the pPD-1S-PEG, pPD-1G-PEG, and aPD-L1-PEG surfaces. c) BLI measurements of nonspecific adsorption of pPD-1S and pPD-1G onto BSA-immobilized probes. d) Adhesion force mapping by AFM on the pPD-1G-PEG and aPD-L1-PEG surfaces using PD-L1-immobilized probes. e) Histograms of rupture forces determined by AFM adhesion force mapping. f) Schematic illustration of surface-immobilized pPD-1G and aPD-L1. g) Cell capture efficiency of pPD-1G-PEG surfaces tested using 786-O, MDA-MB-231, ACHN, MCF-7, and Jurkat cells. h) Surface PD-L1 expression in the cell lines evaluated using IHC staining. Note that all cell capture experiments were conducted at a flow rate of 50 μL/min, which corresponds to a maximum shear stress of 0.36 dyne/cm^2.

whole antibody counterpart (aPD-L1-PEG). When applied to a rolling-based CTC capture system, pPD-1G-PEG captured significantly more PD-L1-expressing cancer cells than aPD-L1-PEG (77.8 ± 9.3% vs. 50.8 ± 6.9%; $p = 0.016$) (Fig. 4b). The AFM adhesion force mapping technique was further utilized to quantitatively measure the difference in binding strength between the two capture surfaces. Probe-immobilized PD-L1 exhibited a stronger interaction with the pPD-1G-PEG surface (934 ± 374 pN) than with the aPD-L1-PEG surface (728 ± 379 pN; $p < 0.001$) (Fig. 4d and e). The adhesion energy, which refers to the work required for the dissociation of a probe from a surface, was also 2.12-fold ($p < 0.001$) higher on the pPD-1G-PEG surface than on the aPD-L1-PEG surface (Fig. S10). This stronger PD-L1 binding capacity of the pPD-1G-PEG surface could be attributed to the difference in structural properties between the two capture agents. Peptides would be more densely conjugated to the capture surface with the PD-L1-binding sites facing upward, whereas large antibodies would bind sparsely to the surface in a pseudorandom orientation (Fig. 4f).

Evaluation of the cell capture capability tested using three additional cell lines, PD-L1^{High} MDA-MB-231, PD-L1^{Mid} ACHN, and PD-L1^{Low} MCF-7, further revealed a strong correlation between PD-L1 expression on the cell surface and capture efficiency (Fig. 4g). This indicates the high PD-L1 selectivity of our peptide-based system. Notably, PD-L1 expression in each cell line was confirmed using IHC staining and Western blot analysis (Figs. 4h, S11, and S12). We also tested the serum stability of the pPD-1G peptides prior to their clinical application. As shown in Figs. S13 and 20 min of preincubation in fetal bovine serum (FBS) or human serum did not affect the cell binding behavior of the peptides. Furthermore, the capture efficiency of 786-O cells spiked into the peripheral blood mononuclear cell (PBMC) layer showed no difference (73.1 ± 15.1%; $p = 0.669$) from that of 786-O cells spiked into culture medium,

demonstrating the potential clinical applicability of our system.

3.4. pPD-1G-PEG enables highly sensitive detection of PD-L1-expressing exosomes

We further assessed the pPD-1-functionalized surfaces for their versatility in detecting an additional biomarker, tumor-derived exosomes. The pPD-1G-PEG surface was compared with the aPD-L1-PEG surface in terms of the isolation of PD-L1-expressing exosomes using four different assays: nanoparticle tracking analysis (NTA), a bicinchoninic acid (BCA) protein assay, a membrane staining assay, and AFM analysis. Tumor cell-derived exosomes (2×10^8 vesicles/mL; 2 μL/mm^2) were incubated on either the pPD-1G-PEG, aPD-L1-PEG, or PEGylated surface for 3 h, and the exosomes captured on each surface were quantitatively measured. By NTA, the capture of 786-O-derived exosomes was measured to be ~1.60-fold higher on the pPD-1G-PEG surface than on the PEGylated surface. However, this increase was only ~1.33-fold on the aPD-L1-PEG surface ($p = 0.037$ for pPD-1G-PEG vs. aPD-L1-PEG) (Fig. 5a). This pattern was also observed for the samples with a 10-fold higher exosome concentration, as the pPD-1G-PEG surface demonstrated an ~1.47-fold increase in exosome capture compared with that of the aPD-L1-PEG surface (Fig. S14). Particle size analysis using NTA (Fig. S15) also revealed that the particles captured on the pPD-1G-PEG or aPD-L1-PEG surface had average sizes similar to those of typical exosomes, whereas unbound particles were more likely to be larger cellular debris. This effect was more prominent on the pPD-1G-PEG surface than on the aPD-L1 surface (Fig. S15). Notably, all three surfaces, however, exhibited similar levels of exosome capture with no difference in the average size of the captured particles when tested with exosomes derived from PD-L1^{negative} Jurkat cells (Fig. S16).

Additional quantitative analyses also indicated that pPD-1G-PEG isolated PD-L1-expressing exosomes more effectively than aPD-L1-PEG. The BCA assay results (Fig. 5b) revealed the amount of protein extracted from the exosomes captured on the PEG, aPD-L1-PEG, and pPD-1G-PEG surfaces to be 24.8 ± 0.9 ng/mm^2, 44.7 ± 7.0 ng/mm^2, and 61.6 ± 5.0 ng/mm^2, respectively ($p = 0.027$ for aPD-L1-PEG vs. pPD-1G-PEG). Similarly, labeling with a lipophilic green fluorescent dye (DiO) (Fig. 5c) showed that more exosomes were captured on the pPD-1G-PEG surface than on the aPD-L1-PEG surface (16.2 ± 2.3 vs. 13.6 ± 2.4 a.u.), although the difference was not statistically significant ($p = 0.114$). Surface topology analysis using AFM (Fig. 5d and e) also revealed a clear difference in the number of exosomes captured, as the root mean square (rms) values representing the quantitative roughness of the pPD-1G-PEG and aPD-L1-PEG surfaces were 5.2 ± 1.2 nm and 3.0 ± 0.2 nm, respectively ($p = 0.039$). We also noted that the number of exosomes captured on the pPD-1G-PEG surface correlated with the PD-L1 expression level in their parental cell lines (Fig. 5f), demonstrating the high PD-L1 selectivity of our capture system.

3.5. pPD-1G-PEG facilitates the capture of CTCs/Exosomes from human samples

Our results collectively indicated that pPD-1G-PEG is the most efficient peptide for capturing tumor cells and tumor-derived exosomes *in vitro*, leading us to test the ability of the engineered peptide implemented in our previously developed rolling-based capture system to isolate CTCs from human PBMCs (Bu et al., 2020b; Myung et al. 2015, 2018). The surface-captured cells exhibiting the CK^{High}/CD45$^-$/DAPI$^+$ signature based on immunofluorescent labeling were counted as CTCs (Fig. 6a) (Bu et al., 2020b). A preliminary clinical pilot study with baseline samples from eight patients and three healthy donors revealed the high potential diagnostic capability of our system (Table S1). Using pPD-1G-PEG, CTCs were detected in all patient samples, with an average of 19.1 ± 11.1 cells/mL, whereas only 0.3 ± 0.3 cells/mL were found in

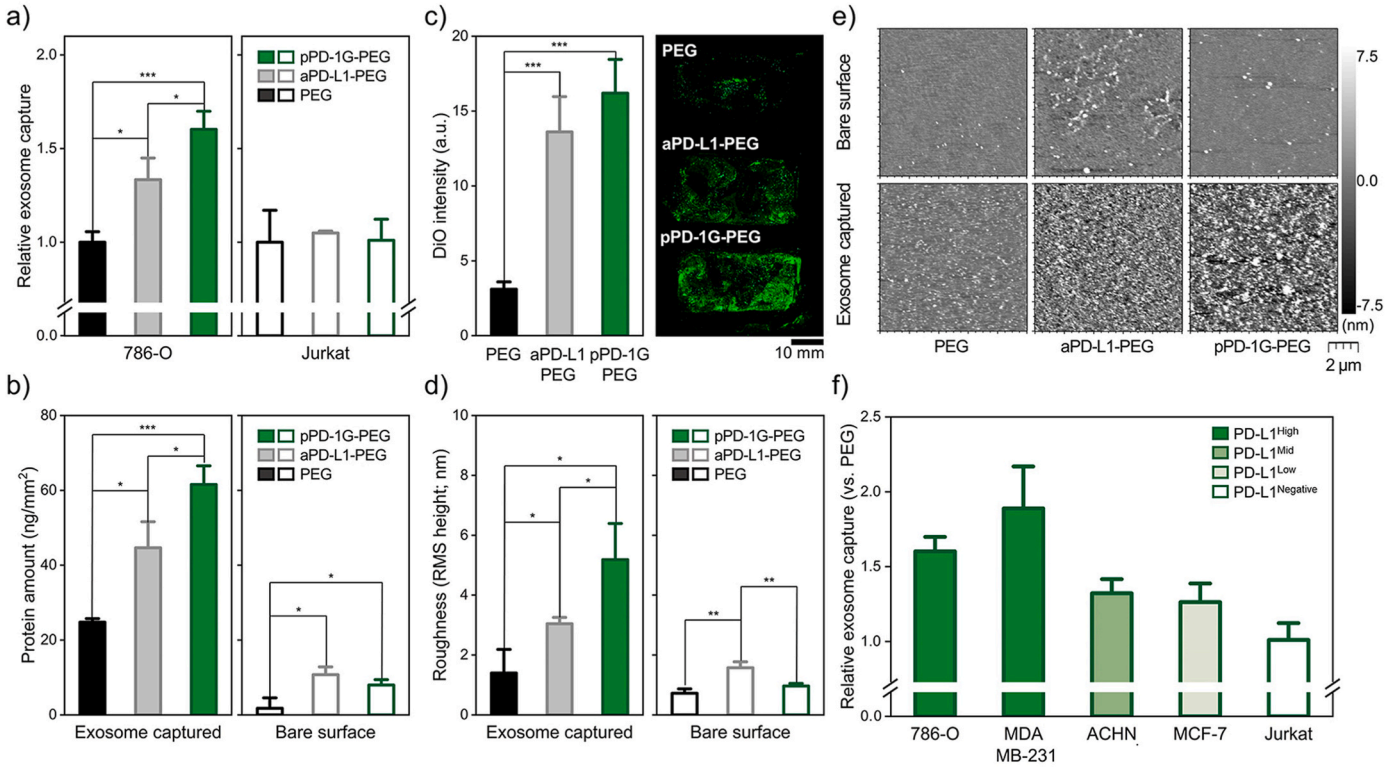

Fig. 5. Engineered pPD-1 peptides (pPD-1G) for effective capture of PD-L1-expressing exosomes: Four different *in vitro* assays were utilized to compare the exosome capture capabilities of the pPD-1G-PEG and aPD-L1-PEG surfaces: a) nanoparticle tracking analysis (NTA), b) a bicinchoninic acid (BCA) protein assay, c) a membrane staining assay, and d, e) AFM topological analysis. f) The capture capability of the pPD-1G-PEG surface was also analyzed for exosomes derived from 786-O, MDA-MB-231, ACHN, MCF-7, and Jurkat cells.

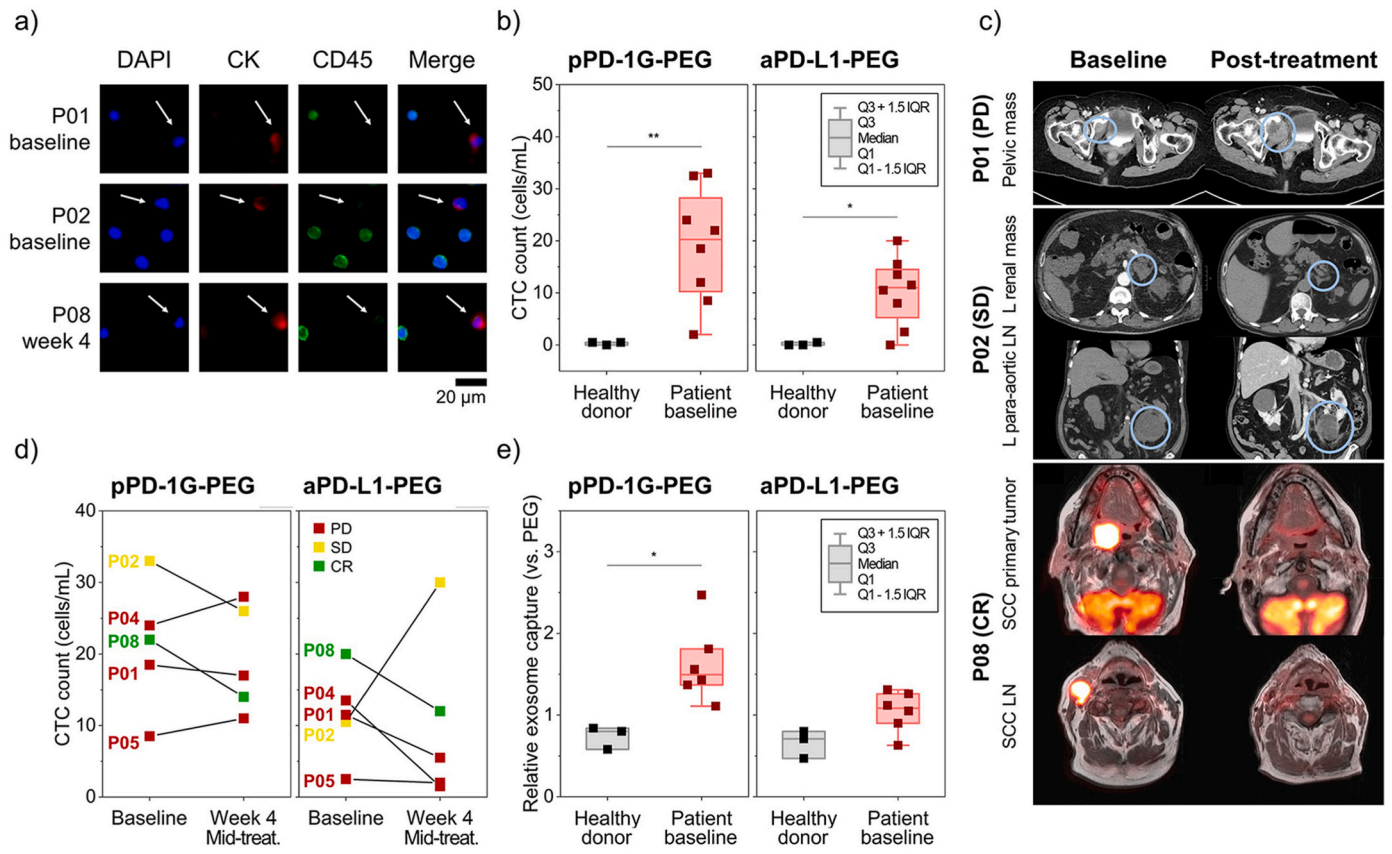

Fig. 6. CTCs and exosomes isolated from human blood samples using surface-immobilized pPD-1G-PEG and aPD-L1-PEG: a) Representative IHC images of the captured CTCs stained for CK (red), for CD45 (green), and with DAPI (blue). b) Diagnostic value of CTCs captured on the pPD-1G-PEG and aPD-L1-PEG surfaces, as demonstrated by comparing the number of CTCs detected in baseline samples from eight patients (P01, P02, P03, P04, P05, P07, P08, and P09) and samples from healthy donors. c) Computed tomography (CT) and positron emission tomography/magnetic resonance imaging (PET/MRI) scans obtained at baseline and post-treatment (3–4 months after the first day of treatment) for P01, P02, and P08. d) Pilot study results for differences in the CTC count in 5 patients treated with immunotherapy. Changes in the CTC count were analyzed during immunotherapy. e) Diagnostic value of exosomes captured on the pPD-1G-PEG and aPD-L1-PEG surfaces. Statistical analysis was conducted by comparing the amount of exosomal proteins detected in samples from six patients with nonrecurrent tumors at baseline (P07, P08, P09, P10, P14, and P16) and three healthy donors.

healthy individuals ($p = 0.002$) (Fig. 6b). For aPD-L1-PEG, 10.2 ± 6.6 CTCs/mL were detected in the same patient samples, resulting in a lower statistical significance (healthy donors: 0.2 ± 0.3 CTCs/mL; $p = 0.032$). Blood specimens were collected at the midpoint of treatment (4 weeks after the first day of treatment; $n = 5$) to validate the predictive/prognostic capabilities of our system (Fig. 6c and d). The number of CTCs decreased from 22 to 14 CTCs/mL after four weeks of treatment (36% decrease) in patient #08 (P08), who showed a complete response at week 18. However, the number of CTCs decreased by only 21% (from 33 CTCs/mL to 26 CTCs/mL at week 4) for P02, who attained stable disease after 12 weeks of treatment with ipilimumab-nivolumab. In contrast, three patients (P01, P04, and P05) with progressive disease after ICI treatment showed an increase or no marked change (<10% decrease) in the CTC count. For aPD-L1-PEG, the changes in the CTC count were found to be unrelated to the treatment response.

pPD-1G-PEG also outperformed aPD-L1-PEG in isolating exosomes from human plasma. Compared to the PEGylated surface, the pPD-1G-PEG surface detected 1.63-fold more exosomes from patients with nonrecurrent tumors (at baseline) and 26% fewer exosomes from healthy donor samples ($p = 0.018$) (Fig. 6e). For aPD-L1-PEG, the difference was less pronounced, with only a 1.05-fold increase and 34% decrease in the number of exosomes detected in patient and healthy donor samples, respectively ($p = 0.051$). Notably, for healthy donor samples, less exosomes were detected by both the pPD-1G-PEG and aPD-L1-PEG surfaces than by the PEGylated surface, since the peptides or antibodies functionalized on the surfaces spatially block nonspecific adsorption of serum proteins. We also found that the pPD-1G-PEG surface detected significantly greater number of exosomes from the patients with tumor recurrence (P13 and P15) (Table S1), an effect that was not observed on the aPD-L1-PEG surface. Collectively, these results demonstrated the potential for our peptide-based system to be utilized as a diagnostic/prognostic tool for cancer immunotherapy. However, it should be noted that our results using a small number of patients are encouraging but not conclusive. Additional studies based on a larger cohort are currently ongoing, and we are trying to expand our study to analyze the treatment response to various immunotherapies, which should provide more statistically significant data in the future.

4. Discussion

In this study, we integrated three novel engineering strategies to utilize PD-L1-targeting peptides as capture agents for isolating PD-L1-expressing CTCs and exosomes. The optimized peptide sequence on a glass epoxy substrate revealed great potential as a capture agent for the effective detection and isolation of both PD-L1-expressing CTCs and exosomes. Compared to the aPD-L1-PEG surface, the pPD-1G-PEG surface demonstrated increases of ~1.9-fold and ~1.5-fold in the capture of PD-L1-expressing CTCs and exosomes, respectively, from patients' baseline samples. Considering that peptides utilized for liquid biopsy assays typically exhibit weaker binding or lower specificity than their antibody counterparts, our results are surprising (Bai et al., 2014; Liu et al., 2017; Peng et al., 2017). Our engineered pPD-1G-PEG surface

captured more PD-L1^{+} cancer cells than the aPD-L1-PEG surface, a result attributed to differences in structural/modular properties between the two molecules. The novel peptide engineering strategies used in this study enabled the small peptides to be densely immobilized on the capture surface with their orientations controlled to face the target proteins, whereas large antibodies are sparsely distributed on the functionalized surface in a pseudorandom orientation. Due to this random orientation, antibodies immobilized on a solid surface typically exhibit a lower binding capacity than those in solution, as reported elsewhere (Choi et al., 2005). Many attempts have been made to control the orientation of antibodies, for example, leveraging intermediate proteins or modifying the specific regions that do not directly participate in binding interactions (Wu et al., 2004). Although these strategies could potentially be applied to improve the capture of CTCs and exosomes on antibody-immobilized surfaces, they generally require additional chemical/biological modifications that may unnecessarily increase the complexity of surface preparation.

Using AFM, we found that the pPD-1G-PEG surface exploits multivalent interactions more efficiently and forms stronger interactions with PD-L1-expressing cancer cells (or exosomes). Specifically, multivalent interactions were identified by counting the number of discrete dissociation events on FD curves (Fig. S17). (Poellmann et al., 2020) More of the FD curves for the pPD-1G-PEG surface contained multiple rupture events than those for the aPD-L1-PEG surface (45.4% vs. 34.5%). These events enhanced the adhesion of the PD-L1-immobilized probe to the pPD-1G-PEG surface compared to the aPD-L1-PEG surface (Figs. 4 and S10), which was translated into highly -sensitive capture of PD-L1-expressing CTCs and exosomes.

In addition to the high sensitivity for isolating PD-L1-expressing tumor biomarkers, pPD-1G also demonstrated high selectivity toward PD-L1. As described from *in vitro* assays, the capture efficiencies of both cancer cells and cell-derived exosomes were strongly associated with their surface PD-L1 expression (Figs. 4 and 5). As a result, the capture efficiencies of each cell line and exosomes derived from each of these cell lines were strongly correlated with one another (Fig. S18). This strong correlation was also observed in the clinical samples (Fig. S19), as the number of CTCs and the amount of exosomes captured on the pPD-1G-PEG surface exhibited a Pearson correlation coefficient (R) of 0.826 ($p = 0.012$). Such a correlation was also found for the CTCs and exosomes captured on the aPD-L1-PEG surface, but the result was less significant ($R = 0.571$; $p = 0.189$). These findings revealed that our system facilitates the highly selective isolation of PD-L1-expressing CTCs/exosomes.

The clinical accuracy of our system can be further improved by combining the two biomarkers. We established a bimodal CTC/exosome score (Z_{bimode}) by calculating the sum of the normalized CTC counts (Z_{CTC}) and exosome expression levels (Z_{Exo}) from the cohort whose samples were processed using the same pPD-1G-PEG surface for both CTCs and exosomes. As demonstrated in Fig. S20, Z_{bimode} exhibited a higher statistical significance ($p = 0.009$) than both Z_{CTC} ($p = 0.043$) and Z_{Exo} ($p = 0.013$) for differentiating cancer patients from healthy donors. This pattern was also pronounced for the aPD-L1-PEG surface, as Z_{bimode} ($p = 0.044$) outperformed both single tumor biomarkers ($p > 0.100$) in detecting cancer patients. Although one can argue that our result was obtained from only a small number of clinical samples, accumulating evidence in the literature also indicates that combined analysis of two or more tumor biomarkers enhances the diagnostic capability of liquid biopsy assays (Bu et al. 2019, 2021; Lee et al., 2022).

In addition, our engineered peptides can be utilized to facilitate the isolation of other liquid biopsy biomarkers, such as serum PD-L1 proteins. Y. Xing et al. developed novel paper-based biosensors for detecting PD-1 and PD-L1 proteins in human serum and demonstrated the potential clinical use of these serum antigens to help tailor ICIs for patient treatment (Xing et al. 2021, 2022). Our peptides can also be applied as receptors for these sensors and enhance the isolation of serum PD-L1 proteins. Trimodal analysis of CTCs, exosomes, and serum proteins may provide an even more reliable and robust indication of patients' responses to immunotherapy.

Another advantage of utilizing peptides as capture agents is that unstructured, short peptides generally have better thermodynamic stability than antibodies. After 20 min of incubation at 80 °C, the aPD-L1-PEG surface lost its PD-L1-targeting function, as the percentage of retained 786-O cells decreased from ~88% to ~13% ($p < 0.001$) (Fig. S10). In contrast, a high retention efficiency was maintained on the heat-treated pPD-1G-PEG surface (~96%; $p = 0.975$). The pPD-1G-PEG surface also demonstrated resistance to enzymatic degradation better than or similar to that of the aPD-L1-PEG surface. After 20 min of incubation of the aPD-L1-PEG surface with proteinase K, the percentage of retained 786-O cells decreased to ~50% at RT ($p = 0.005$) and ~35% at 37 °C ($p < 0.001$). In contrast, proteinase K did not strongly affect the cell adhesion property of the pPD-1G-PEG surface ($p > 0.191$). However, trypsin decreased the retention percentage by ~79% and ~35% for the pPD-1G-PEG surface at RT and 37 °C, respectively, similar to its effect on the aPD-L1-PEG surface (~80% at RT and ~33% at 37 °C). It should also be noted that there are only a few enzymes that can cleave our PD-L1-targeting peptides compared to large antibodies (i.e., human immunoglobulins) (Table S2). Specifically, since in pPD-1G, the biologically redundant CAARs in pPD-1S are substituted with glycine residues, pPD-1G peptides have even fewer cleavage sites than pPD-1S and pPD-1T peptides. These findings reveal that our newly developed peptides can potentially be employed not only for CTC and exosome capture but also in other therapeutic and biomedical applications.

5. Conclusion

Estimation and/or monitoring of therapeutic responses to immunotherapy has been challenging, primarily due to the lack of real-time biomarkers for treatment responses. To address this issue, this study evaluated and integrated multiple peptide engineering strategies that enhanced the binding avidity and specificity of pPD-1 peptides. First, PEG linkers were employed as spacers between the glass substrate and the peptides, which reduced the nonspecific adsorption of PD-L1^{Negative} Jurkat cells by ~63%. Next, we investigated the effect of peptide folding on the capture of PD-L1-expressing cancer cells by modulating the PEGylation sites in the peptide. AFM analysis and *in vitro* assays suggested that the partially folded pPD-1T-PEG exhibits higher off-rate kinetics, whereas the unstructured pPD-1S-PEG shows a faster association with PD-L1. The faster association was determined to be more effective for capturing PD-L1-expressing cancer cells, as the capture efficiency for 786-O cells was ~1.6-fold higher on the pPD-1S-PEG surface. Finally, the removal of CAARs that are unnecessary for PD-L1 binding further reduced the nonspecific capture of Jurkat cells by ~43%. *In vitro* assays revealed that the optimized pPD-1 (pPD-1G-PEG) configuration on the glass surface captured PD-L1-expressing cancer cells and tumor-derived exosomes with markedly higher efficiency than the aPD-L1-PEG surface. This was translated into highly sensitive capture of CTCs and exosomes from human blood samples, although additional clinical studies with a larger cohort are obviously necessary to draw more solid conclusions regarding the clinical utility of our system. However, our new system with high sensitivity and selectivity toward a specific protein (PD-L1) may clarify the correlation of these two biomarkers with clinical outcome, which would enable the development of a highly accurate bimodal liquid biopsy system for evaluating the response to cancer immunotherapy.

Data availability

Raw data are available upon request to the corresponding author.

CRediT authorship contribution statement

Jiyoon Bu: Conceptualization, Methodology, Investigation,

Validation, Data curation, Formal analysis, Writing – original draft, Writing – review & editing, Visualization, Software, Contributed equally to this work. **Woo-jin Jeong:** Conceptualization, Methodology, Investigation, Validation, Data curation, Formal analysis, Writing – original draft, Writing – review & editing, Visualization, Contributed equally to this work. **Roya Jafari:** Investigation, Software, Writing – original draft. **Luke J. Kubiatowicz:** Formal analysis, Writing – original draft. **Ashita Nair:** Formal analysis, Validation. **Michael J. Poellmann:** Validation, Formal analysis, Writing – original draft. **Rachel S. Hong:** Writing – original draft, Writing – review & editing, Investigation. **Elizabeth W. Liu:** Formal analysis, Investigation, Validation. **Randall H. Owen:** Formal analysis, Investigation. **Piper A. Rawding:** Formal analysis, Writing – original draft, Writing – review & editing. **Caroline M. Hopkins:** Formal analysis, Investigation. **DaWon Kim:** Formal analysis, Writing – review & editing. **Daniel J. George:** Resources, Supervision. **Andrew J. Armstrong:** Resources, Supervision. **Petr Král:** Software, Supervision. **Andrew Z. Wang:** Resources, Supervision, Writing – original draft. **Justine Bruce:** Resources, Supervision. **Tian Zhang:** Resources, Supervision, Writing – original draft. **Randall J. Kimple:** Resources, Supervision, Writing – original draft. **Seungpyo Hong:** Conceptualization, Validation, Resources, Supervision, Writing – original draft.

Declaration of competing interest

The authors declare the following financial interests/personal relationships which may be considered as potential competing interests: SH and AW are co-founders of Capio Biosciences, Inc., a biotech startup that is commercializing CapioCyte™ CTC technology. MP is an employee of Capio Biosciences. TZ has stock ownership/employment (spouse) from Capio Biosciences.

Acknowledgments

This study was partially supported by National Science Foundation (NSF) under grant # DMR-1808251. The authors also acknowledge the partial support from NIAMS/NIH under grant # 1R01AR069541, NIBIB/NIH under grant # 1R21EB022374, the Wisconsin Head & Neck Cancer SPORE Grant (P50-DE026787), and The Falk Medical Research Trust – Catalyst Awards Program.

Appendix A. Supplementary data

Supplementary data to this article can be found online at https://doi.org/10.1016/j.bios.2022.114445.

References

Abdel-Rahman, O., 2016. Correlation between PD-L1 expression and outcome of NSCLC patients treated with anti-PD-1/PD-L1 agents: a meta-analysis. Crit. Rev. Oncol. Hematol. 101, 75–85.

Amaral, M., Kokh, D.B., Bomke, J., Wegener, A., Buchstaller, H.P., Eggenweiler, H.M., Matias, P., Sirrenberg, C., Wade, R.C., Frech, M., 2017. Protein conformational flexibility modulates kinetics and thermodynamics of drug binding. Nat. Commun. 8 (1), 2276.

Anantharaman, A., Friedlander, T., Lu, D., Krupa, R., Premasekharan, G., Hough, J., Edwards, M., Paz, R., Lindquist, K., Graf, R., Jendrisak, A., Louw, J., Dugan, L., Baird, S., Wang, Y., Dittamore, R., Paris, P.L., 2016. Programmed death-ligand 1 (PD-L1) characterization of circulating tumor cells (CTCs) in muscle invasive and metastatic bladder cancer patients. BMC Cancer 16 (1), 744.

Bai, L., Du, Y., Peng, J., Liu, Y., Wang, Y., Yang, Y., Wang, C., 2014. Peptide-based isolation of circulating tumor cells by magnetic nanoparticles. J. Mater. Chem. B 2 (26), 4080–4088.

Borghaei, H., Paz-Ares, L., Horn, L., Spigel, D.R., Steins, M., Ready, N.E., Chow, L.Q., Vokes, E.E., Felip, E., Holgado, E., Barlesi, F., Kohlhäufl, M., Arrieta, O., Burgio, M. A., Fayette, J., Lena, H., Poddubskaya, E., Gerber, D.E., Gettinger, S.N., Rudin, C.M., Rizvi, N., Crinò, L., Blumenschein, G.R., Antonia, S.J., Dorange, C., Harbison, C.T., Graf Finckenstein, F., Brahmer, J.R., 2015. Nivolumab versus docetaxel in advanced nonsquamous non-small-cell lung cancer. N. Engl. J. Med. 373 (17), 1627–1639.

Bu, J., Cho, Y.-H., Han, S.-W., 2017a. Enhancement of isolation sensitivity for the viable heterogeneous circulating tumor cells swelled by hypo-osmotic pressure. RSC Adv. 7 (78), 49684–49693.

Bu, J., Kang, Y.T., Lee, Y.S., Kim, J., Cho, Y.H., Moon, B.I., 2017b. Lab on a fabric: mass producible and low-cost fabric filters for the high-throughput viable isolation of circulating tumor cells. Biosens. Bioelectron. 91, 747–755.

Bu, J., Lee, T.H., Poellmann, M.J., Rawding, P.A., Jeong, W.-J., Hong, R.S., Hyun, S.H., Eun, H.S., Hong, S., 2021. Tri-modal liquid biopsy: combinational analysis of circulating tumor cells, exosomes, and cell-free DNA using machine learning algorithm. Clin. Transl. Med. 11 (8), e499.

Bu, J., Nair, A., Iida, M., Jeong, W.-j., Poellmann, M.J., Mudd, K., Kubiatowicz, L.J., Liu, E.W., Wheeler, D.L., Hong, S., 2020a. An avidity-based PD-L1 antagonist using nanoparticle-antibody conjugates for enhanced immunotherapy. Nano Lett. 20 (7), 4901–4909.

Bu, J., Nair, A., Kubiatowicz, L.J., Poellmann, M.J., Jeong, W.J., Reyes-Martinez, M., Armstrong, A.J., George, D.J., Wang, A.Z., Zhang, T., Hong, S., 2020b. Surface engineering for efficient capture of circulating tumor cells in renal cell carcinoma: from nanoscale analysis to clinical application. Biosens. Bioelectron. 162, 112250.

Bu, J., Shim, J.-E., Lee, T.H., Cho, Y.-H., 2019. Multi-modal liquid biopsy platform for cancer screening: screening both cancer-associated rare cells and cancer cell-derived vesicles on the fabric filters for a reliable liquid biopsy analysis. Nano Converg 6 (1), 39.

Cagno, V., Andreozzi, P., D'Alicarnasso, M., Jacob Silva, P., Mueller, M., Galloux, M., Le Goffic, R., Jones, S.T., Vallino, M., Hodek, J., Weber, J., Sen, S., Janeček, E.R., Bekdemir, A., Sanavio, B., Martinelli, C., Donalisio, M., Rameix Welti, M.A., Eleouet, J.F., Han, Y., Kaiser, L., Vukovic, L., Tapparel, C., Král, P., Krol, S., Lembo, D., Stellacci, F., 2018. Broad-spectrum non-toxic antiviral nanoparticles with a virucidal inhibition mechanism. Nat. Mater. 17 (2), 195–203.

Charles, P.T., Stubbs, V.R., Soto, C.M., Martin, B.D., White, B.J., Taitt, C.R., 2009. Reduction of non-specific protein adsorption using poly(ethylene) glycol (PEG) modified polyacrylate hydrogels in immunoassays for staphylococcal enterotoxin B detection. Sensors 9 (1), 645–655.

Choi, J.-W., Chun, B.S., Oh, B.-K., Lee, W., Lee, W.H., 2005. Fabrication of DNA–protein conjugate layer on gold-substrate and its application to immunosensor. Colloids Surf. B Biointerfaces 40 (3), 173–177.

Esposito, A., Criscitiello, C., Locatelli, M., Milano, M., Curigliano, G., 2016. Liquid biopsies for solid tumors: understanding tumor heterogeneity and real time monitoring of early resistance to targeted therapies. Pharmacol. Ther. 157, 120–124.

Ferris, R.L., Blumenschein, G., Fayette, J., Guigay, J., Colevas, A.D., Licitra, L., Harrington, K., Kasper, S., Vokes, E.E., Even, C., Worden, F., Saba, N.F., Iglesias Docampo, L.C., Haddad, R., Rordorf, T., Kiyota, N., Tahara, M., Monga, M., Lynch, M., Geese, W.J., Kopit, J., Shaw, J.W., Gillison, M.L., 2016. Nivolumab for recurrent squamous-cell carcinoma of the head and neck. N. Engl. J. Med. 375 (19), 1856–1867.

Friddle, R.W., Noy, A., De Yoreo, J.J., 2012. Interpreting the widespread nonlinear force spectra of intermolecular bonds. Proc. Natl. Acad. Sci. U. S. A. 109 (34), 13573.

Halse, H., Colebatch, A.J., Petrone, P., Henderson, M.A., Mills, J.K., Snow, H., Westwood, J.A., Sandhu, S., Raleigh, J.M., Behren, A., Cebon, J., Darcy, P.K., Kershaw, M.H., McArthur, G.A., Gyorki, D.E., Neeson, P.J., 2018. Multiplex immunohistochemistry accurately defines the immune context of metastatic melanoma. Sci. Rep. 8 (1), 11158.

Han, Y., Král, P., 2020. Computational design of ACE2-based peptide inhibitors of SARS-CoV-2. ACS Nano 14 (4), 5143–5147.

Hoffman, L., Wang, X., Sanabria, H., Cheung, M.S., Putkey, J.A., Waxham, M.N., 2015. Relative cosolute size influences the kinetics of protein-protein interactions. Biophys. J. 109 (3), 510–520.

Hsu, H.J., Sen, S., Pearson, R.M., Uddin, S., Kral, P., Hong, S., 2014. Poly(ethylene glycol) corona chain length controls end-group-dependent cell interactions of dendron micelles. Macromolecules 47 (19), 6911–6918.

Jarvis, T.R., Chughtai, B., Kaplan, S.A., 2015. Testosterone and benign prostatic hyperplasia. Asian J. Androl. 17 (2), 212–216.

Jeong, W.-j., Bu, J., Han, Y., Drelich, A.J., Nair, A., Král, P., Hong, S., 2020. Nanoparticle conjugation stabilizes and multimerizes β-hairpin peptides to effectively target PD-1/PD-L1 β-sheet-rich interfaces. J. Am. Chem. Soc. 142 (4), 1832–1837.

Jeong, W.J., Bu, J., Jafari, R., Rehak, P., Kubiatowicz, L.J., Drelich, A.J., Owen, R.H., Nair, A., Rawding, P.A., Poellmann, M.J., Hopkins, C.M., Král, P., Hong, S., 2022. Hierarchically multivalent peptide-nanoparticle architectures: a systematic approach to engineer surface adhesion. Adv. Sci. 9 (4), e2103098.

Jeong, W.J., Han, S., Park, H., Jin, K.S., Lim, Y.B., 2014. Multiplexing natural orientation: oppositely directed self-assembling peptides. Biomacromolecules 15 (6), 2138–2145.

Kerr, K.M., 2018. The PD-L1 immunohistochemistry biomarker: two steps forward, one step back? J. Thorac. Oncol. 13 (3), 291–294.

Kowanetz, M., Zou, W., Gettinger, S.N., Koeppen, H., Kockx, M., Schmid, P., Kadel, E.E., Wistuba, I., Chaft, J., Rizvi, N.A., Spigel, D.R., Spira, A., Hirsch, F.R., Cohen, V., Smith, D., Boyd, Z., Miley, N., Flynn, S., Leveque, V., Shames, D.S., Ballinger, M., Mocci, S., Shankar, G., Funke, R., Hampton, G., Sandler, A., Amler, L., Mellman, I., Chen, D.S., Hegde, P.S., 2018. Differential regulation of PD-L1 expression by immune and tumor cells in NSCLC and the response to treatment with atezolizumab (anti-PD-L1). Proc. Natl. Acad. Sci. U. S. A. 115 (43). E10119-E10126.

Kulasinghe, A., Perry, C., Kenny, L., Warkiani, M.E., Nelson, C., Punyadeera, C., 2017. PD-L1 expressing circulating tumour cells in head and neck cancers. BMC Cancer 17 (1), 333.

Lau, J.L., Dunn, M.K., 2018. Therapeutic peptides: historical perspectives, current development trends, and future directions. Bioorg. Med. Chem. 26 (10), 2700–2707.

Leader, B., Baca, Q.J., Golan, D.E., 2008. Protein therapeutics: a summary and pharmacological classification. Nat. Rev. Drug Discov. 7 (1), 21–39.
Lee, T., Rawding, P.A., Bu, J., Hyun, S., Rou, W., Jeon, H., Kim, S., Lee, B., Kubiatowicz, L.J., Kim, D., Hong, S., Eun, H., 2022. Machine-Learning-based clinical biomarker using cell-free DNA for hepatocellular carcinoma (HCC). Cancers 14 (9), 2061.
Liu, X.-r., Shao, B., Peng, J.-x., Li, H.-p., Yang, Y.-l., Kong, W.-y., Song, G.-h., Jiang, H.-f., Liang, X., Yan, Y., 2017. Identification of high independent prognostic value of nanotechnology based circulating tumor cell enumeration in first-line chemotherapy for metastatic breast cancer patients. Breast 32, 119–125.
MacKerell, A.D., Bashford, D., Bellott, M., Dunbrack, R.L., Evanseck, J.D., Field, M.J., Fischer, S., Gao, J., Guo, H., Ha, S., et al., 1998. All-atom empirical potential for molecular modeling and dynamics studies of proteins. J. Phys. Chem. B 102 (18), 3586–3616.
Mazel, M., Jacot, W., Pantel, K., Bartkowiak, K., Topart, D., Cayrefourcq, L., Rossille, D., Maudelonde, T., Fest, T., Alix-Panabières, C., 2015. Frequent expression of PD-L1 on circulating breast cancer cells. Mol Oncol 9 (9), 1773–1782.
Miles, J.A., Yeo, D.J., Rowell, P., Rodriguez-Marin, S., Pask, C.M., Warriner, S.L., Edwards, T.A., Wilson, A.J., 2016. Hydrocarbon constrained peptides - understanding preorganisation and binding affinity. Chem. Sci. 7 (6), 3694–3702.
Myung, J.H., Eblan, M.J., Caster, J.M., Park, S.J., Poellmann, M.J., Wang, K., Tam, K.A., Miller, S.M., Shen, C., Chen, R.C., Zhang, T., Tepper, J.E., Chera, B.S., Wang, A.Z., Hong, S., 2018. Multivalent binding and biomimetic cell rolling improves the sensitivity and specificity of circulating tumor cell capture. Clin. Cancer Res. 24 (11), 2539–2547.
Myung, J.H., Roengvoraphoj, M., Tam, K.A., Ma, T., Memoli, V.A., Dmitrovsky, E., Freemantle, S.J., Hong, S., 2015. Effective capture of circulating tumor cells from a transgenic mouse lung cancer model using dendrimer surfaces immobilized with anti-EGFR. Anal. Chem. 87 (19), 10096–10102.
Oliveira-Costa, J.P., de Carvalho, A.F., da Silveira, d.G., Amaya, P., Wu, Y., Park, K.J., Gigliola, M.P., Lustberg, M., Buim, M.E., Ferreira, E.N., Kowalski, L.P., Chalmers, J. J., Soares, F.A., Carraro, D.M., Ribeiro-Silva, A., 2015. Gene expression patterns through oral squamous cell carcinoma development: PD-L1 expression in primary tumor and circulating tumor cells. Oncotarget 6 (25), 20902–20920.
Pardoll, D.M., 2012. The blockade of immune checkpoints in cancer immunotherapy. Nat. Rev. Cancer 12 (4), 252–264.
Peng, J., Zhao, Q., Zheng, W., Li, W., Li, P., Zhu, L., Liu, X., Shao, B., Li, H., Wang, C., Yang, Y., 2017. Peptide-functionalized nanomaterials for the efficient isolation of HER2-positive circulating tumor cells. ACS Appl. Mater. Interfaces 9 (22), 18423–18428.
Phillips, J.C., Braun, R., Wang, W., Gumbart, J., Tajkhorshid, E., Villa, E., Chipot, C., Skeel, R.D., Kalé, L., Schulten, K., 2005. Scalable molecular dynamics with NAMD. J. Comput. Chem. 26 (16), 1781–1802.
Poellmann, M.J., Nair, A., Bu, J., Kim, J.K.H., Kimple, R.J., Hong, S., 2020. Immunoavidity-based capture of tumor exosomes using poly(amidoamine) dendrimer surfaces. Nano Lett. 20 (8), 5686–5692.
Ribas, A., Wolchok, J.D., 2018. Cancer immunotherapy using checkpoint blockade. Science 359 (6382), 1350–1355.
Rogers, J.M., Oleinikovas, V., Shammas, S.L., Wong, C.T., De Sancho, D., Baker, C.M., Clarke, J., 2014a. Interplay between partner and ligand facilitates the folding and binding of an intrinsically disordered protein. P Natl. Acad. Sci. USA 111 (43), 15420–15425.
Rogers, J.M., Wong, C.T., Clarke, J., 2014b. Coupled folding and binding of the disordered protein PUMA does not require particular residual structure. J. Am. Chem. Soc. 136 (14), 5197–5200.
Sargeant, T.D., Rao, M.S., Koh, C.Y., Stupp, S.I., 2008. Covalent functionalization of NiTi surfaces with bioactive peptide amphiphile nanofibers. Biomaterials 29 (8), 1085–1098.
Sen, S., Han, Y., Rehak, P., Vuković, L., Král, P., 2018. Computational studies of micellar and nanoparticle nanomedicines. Chem. Soc. Rev. 47 (11), 3849–3860.
Shoemaker, B.A., Portman, J.J., Wolynes, P.G., 2000. Speeding molecular recognition by using the folding funnel: the fly-casting mechanism. Proc. Natl. Acad. Sci. U. S. A. 97 (16), 8868–8873.
Steinert, G., Schölch, S., Niemietz, T., Iwata, N., García, S.A., Behrens, B., Voigt, A., Kloor, M., Benner, A., Bork, U., Rahbari, N.N., Büchler, M.W., Stoecklein, N.H., Weitz, J., Koch, M., 2014. Immune escape and survival mechanisms in circulating tumor cells of colorectal cancer. Cancer Res. 74 (6), 1694–1704.
Ulrich, B.C., Guibert, N., 2018. Non-invasive assessment of tumor PD-L1 status with circulating tumor cells. Ann. Transl. Med. 6 (Suppl. 1), S48.
Waqas, M., Jeong, W.J., Lee, Y.J., Kim, D.H., Ryou, C., Lim, Y.B., 2017. pH-dependent in-cell self-assembly of peptide inhibitors increases the anti-prion activity while decreasing the cytotoxicity. Biomacromolecules 18 (3), 943–950.
Wu, G., Barth, R.F., Yang, W., Chatterjee, M., Tjarks, W., Ciesielski, M.J., Fenstermaker, R.A., 2004. Site-specific conjugation of boron-containing dendrimers to anti-EGF receptor monoclonal antibody cetuximab (IMC-C225) and its evaluation as a potential delivery agent for neutron capture therapy. Bioconjugate Chem. 15 (1), 185–194.
Xing, Y., Liu, J., Luo, J., Ming, T., Yang, G., Sun, S., Xu, S., Li, X., He, E., Kong, F., Yan, S., Yang, Y., Cai, X., 2022. A dual-channel intelligent point-of-care testing system for soluble programmed death-1 and programmed death-ligand 1 detection based on folding paper-based immunosensors. ACS Sens. 7 (2), 584–592.
Xing, Y., Liu, J., Sun, S., Ming, T., Wang, Y., Luo, J., Xiao, G., Li, X., Xie, J., Cai, X., 2021. New electrochemical method for programmed death-ligand 1 detection based on a paper-based microfluidic aptasensor. Bioelectrochemistry 140, 107789.
Xiong, N., Zhao, Y., Dong, X., Zheng, J., Sun, Y., 2017. Design of a molecular hybrid of dual peptide inhibitors coupled on AuNPs for enhanced inhibition of amyloid β-protein aggregation and cytotoxicity. Small 13 (13).
Xu, J., Zhang, Y., Jia, R., Yue, C., Chang, L., Liu, R., Zhang, G., Zhao, C., Zhang, Y., Chen, C., Wang, Y., Yi, X., Hu, Z., Zou, J., Wang, Q., 2019. Anti-PD-1 antibody SHR-1210 combined with apatinib for advanced hepatocellular carcinoma, gastric, or esophagogastric junction cancer: an open-label, dose escalation and expansion study. Clin. Cancer Res. 25 (2), 515.
Yu, H., Boyle, T.A., Zhou, C., Rimm, D.L., Hirsch, F.R., 2016. PD-L1 expression in lung cancer. J. Thorac. Oncol. 11 (7), 964–975.
Yue, C., Jiang, Y., Li, P., Wang, Y., Xue, J., Li, N., Li, D., Wang, R., Dang, Y., Hu, Z., Yang, Y., Xu, J., 2018. Dynamic change of PD-L1 expression on circulating tumor cells in advanced solid tumor patients undergoing PD-1 blockade therapy. OncoImmunology 7 (7), e1438111.